

# Assessing the retrieval of cloud properties from radiation measurements over snow and ice

P. Kuipers Munneke,\* C. H. Reijmer and M. R. van den Broeke

<sup>a</sup> *Institute for Marine and Atmospheric Research, Utrecht University, Utrecht, The Netherlands*

**ABSTRACT:** We critically review and improve a simple method to extract year-round records of cloud optical thickness from radiation measurements made by automatic weather stations (AWSs) over snow and ice surfaces. A 'longwave-equivalent cloudiness',  $N_e$ , obtained from longwave radiation measurements, is combined with the effective cloud optical thickness,  $\tau$ , from shortwave data, to obtain consistent, year-round information on cloud properties. The method is applied to radiation data from six AWSs in Dronning Maud Land, Antarctica, and the ablation area of the West-Greenland ice sheet. The good correlation between daily-mean  $N_e$  and  $\tau$  for all locations ( $0.77 < r < 0.94$ ) shows that shortwave radiative properties of clouds can be inferred using longwave radiation even in the absence of solar radiation itself. An error analysis shows that retrievals of  $\tau$  are sensitive to the quality of the input data, but accurate to about 21% for hourly values, 11% for daily means, and about 6% for monthly means. As three applications of the method presented above, we discuss the influence of clouds on the radiation budget (Application I), the relation between cloud cover and broadband albedo (Application II) at the six AWS locations, and we demonstrate the possibility to detect trends in  $\tau$  in longer data series (Application III). About one-third of the attenuation of solar radiation by clouds is compensated by multiple reflections between the high-albedo surface and the cloud base (Application I). Cloudy-sky surface albedo is higher than the clear-sky albedo for snow surfaces but not for ice (Application II); over snow surfaces, clouds deplete near-infrared (IR) radiation and thus increase the broadband albedo. Ice surfaces have a much lower albedo for visible radiation, weakening this enrichment of visible radiation and thus the increase of broadband albedo. The method is used to detect a trend in  $\tau$  of  $-0.40 \pm 0.15 \text{ y}^{-1}$  in the 1995–2004 time series from Neumayer, Antarctica (Application III). Copyright © 2010 Royal Meteorological Society

KEY WORDS cloud optical thickness; cloud cover; AWS; radiation; snow and ice; emissivity

Received 18 May 2009; Revised 12 January 2010; Accepted 14 January 2010

## 1. Introduction

The influence of Earth's climate on glaciers and ice sheets is enforced through the surface energy budget (SEB), whose dominant terms are the longwave and shortwave radiative fluxes. The SEB strongly influences the summer surface mass balance of glaciers and ice sheets in their ablation areas, as it largely determines the rate and amount of melt. If meltwater runoff exceeds mass gain by precipitation, sea level will rise. Small glaciers have been contributing to sea-level rise in this way already since the Little Ice Age (e.g. Dyurgerov and Meier, 2005). Recent studies indicate that the Greenland ice sheet is also contributing to sea-level rise (Shepherd and Wingham, 2007; Van den Broeke *et al.*, 2009), both by means of a decreasing surface mass balance (Box *et al.*, 2006) and through ice-dynamical effects that are possibly triggered by meltwater input (Rignot *et al.*, 2008). Knowledge of the SEB of glaciers and ice sheets is therefore important.

The SEB is greatly altered in the presence of clouds. The longwave radiation emitted to the surface will

increase, since the emissivity of clouds is higher than that of a clear sky. The shortwave radiation field is rather complex in the presence of clouds, especially over highly reflective surfaces such as snow and ice. First of all, clouds reduce the incoming radiation flux by reflection and absorption. Secondly, the radiation that passes through the cloud will be subject to multiple reflections between the surface and the cloud base (Ångström and Tryselius, 1934; Schneider and Dickinson, 1976; Shine, 1984). Since the spectral albedo of snow (and ice) and the absorption of radiation by clouds are both strongly dependent on wavelength (Liljequist, 1956; Wiscombe and Warren, 1980), the magnitude of cloud effects is also very much wavelength-dependent—clouds not only alter the intensity, but also the spectral composition of the solar radiation arriving at the surface. At the same time, spectrally-integrated (broadband) albedo has been observed to increase in the presence of clouds (Liljequist, 1956; Ambach, 1974). All these phenomena have competing effects on the shortwave radiation budget of the snow surface.

An outstanding problem in the study of clouds is the lack of cloud observations over ice sheets. From satellite data, it is difficult to infer properties of clouds because

\* Correspondence to: P. Kuipers Munneke, Institute for Marine and Atmospheric Research, Utrecht University, PO Box 80005, NL-3508 TA Utrecht, The Netherlands. E-mail: p.kuipersmunneke@uu.nl

clouds and snow appear very similar both in the solar spectrum as in their thermal properties (e.g. Town *et al.*, 2007). This hampers the study of clouds over ice sheets. The increasing amount of automatic weather stations (AWSs) on glaciers and ice sheets (Stearns and Wendler, 1988; Allison *et al.*, 1993; Van den Broeke *et al.*, 2004a, 2008) are a possibly valuable source of information from remote locations, that could make more data on cloud properties available.

The attempt to obtain cloud properties in polar regions using ground-based measurements is not new. Mahesh *et al.* (2001) use a Fourier transform interferometer to determine cloud optical thickness at South Pole station. Long and Ackerman (2000) present a method to estimate cloud fraction ( $N$ ) using global and diffuse solar radiation measurements, which limits the application to daytime periods, and to locations where diffuse shortwave radiation is measured. Marty and Philipona (2000) present the Clear-Sky Index to separate clear and cloudy skies using longwave radiation measurements, the derivation of which is based, to a large extent, on Konzelmann *et al.* (1994). Dürr and Philipona (2004) extend the Clear-Sky Index to an algorithm that retrieves  $N$  from downwelling longwave measurements. A caveat of the traditional cloud fraction  $N$ , be it observed by a meteorologist or retrieved using an algorithm, is that it does not necessarily provide an accurate description of the radiative properties of the cloud cover.

In the method central in this paper, a ‘longwave-equivalent’ cloudiness  $N_e$  is determined from the apparent emissivity of the sky, and from surface temperature. Similarly, shortwave radiation measurements can be used to obtain the cloud optical thickness,  $\tau$  (Stephens, 1984), following a parameterization developed by Fitzpatrick

*et al.* (2004). Cloud optical thickness is defined in terms of cloud microphysical parameters and is a measure for the amount of radiation that is attenuated by the cloud. Combining the parameterization by Fitzpatrick *et al.* (2004) and the retrieval of  $N_e$ , a simple method is obtained that makes use of radiation measurements from AWSs over snow and ice surfaces to gain knowledge about year-round radiative cloud properties. This method was first used by Van den Broeke *et al.* (2008) to determine cloud optical properties over Greenland stations, and by Giesen *et al.* (2009) for Midtdalsbreen and Storbreen, two glaciers in southern Norway.

In this paper, we will review the method, present some improvements, and subject the method to a critical review of potential uncertainties. As a final part, we demonstrate the versatility of the method in three different applications (section 4). The method can be useful to those who wish to extend the amount of information that can be gained from their AWSs, or to those who are looking for validation data of satellite retrievals of cloud optical thickness.

## 2. Data and methods

### 2.1. Description of data

We use data from six locations, five of which are continuously recording AWSs—three in Greenland and two in Antarctica—and the sixth is the manned BSRN [Baseline Surface Radiation Network, (Ohmura *et al.*, 1998)] station Neumayer in Antarctica (Figure 1). A short characterization of each of these locations and corresponding data sets is given in Table I. The AWSs, which are part of a larger network of sites (Van den

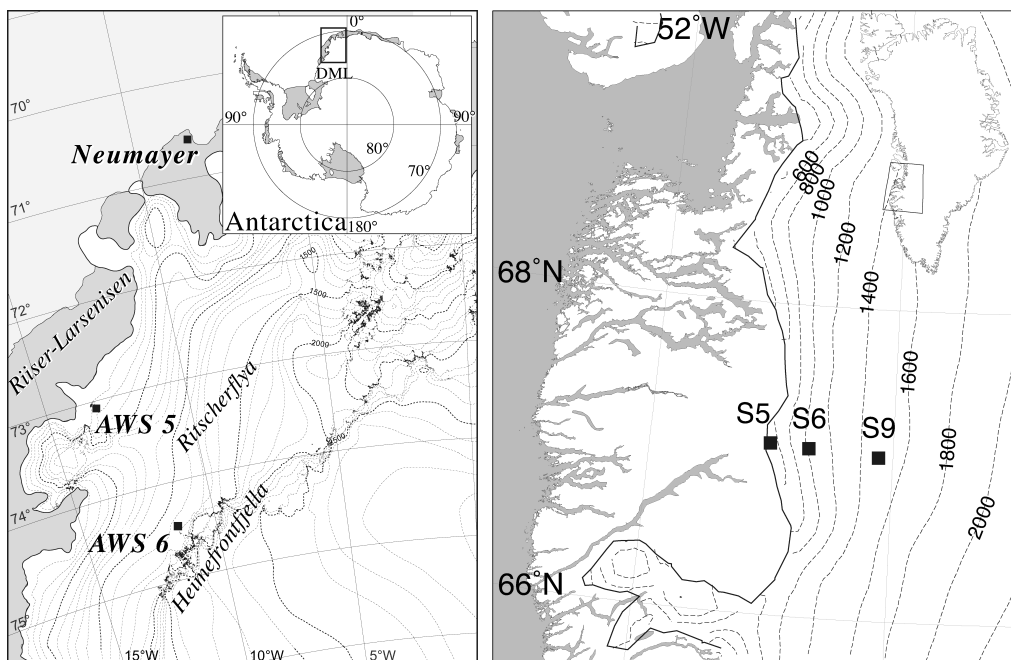


Figure 1. Maps showing the locations of the AWSs and Neumayer Station on Antarctica and Greenland. (a) In Antarctica, 100 m height contours are plotted. (b) In Greenland, 200 m height contours are plotted.

Table I. Specifications for the data sets used in this study.

|                                 | Antarctica            |                    |                    | Greenland         |                   |                    |
|---------------------------------|-----------------------|--------------------|--------------------|-------------------|-------------------|--------------------|
|                                 | Neumayer              | AWS 5              | AWS 6              | S5                | S6                | S9                 |
| Latitude                        | 70 37' S              | 73 06' S           | 74 29' S           | 67 06' N          | 67 05' N          | 67 03' N           |
| Longitude                       | 8 22' W               | 13 10' W           | 11 31' W           | 50 07' W          | 49 23' W          | 48 14' W           |
| Altitude (m a.s.l.)             | 42                    | 363                | 1160               | 490               | 1020              | 1520               |
| Ice edge dist. (km)             | 5                     | 105                | 280                | 6                 | 38                | 88                 |
| Temperature (°C)                | −15.9 <sup>a</sup>    | −16.4 <sup>b</sup> | −16.6 <sup>b</sup> | −5.5 <sup>c</sup> | −9.8 <sup>c</sup> | −12.6 <sup>c</sup> |
| Pyranometer                     | K&Z <sup>d</sup> CM11 | K&Z CM3            | K&Z CM3            | K&Z CM3           | K&Z CM3           | K&Z CM3            |
| Pyrgeometer Sampl. period (min) | Eppley PIR 1/60       | K&Z CG3 6          | K&Z CG3 6          | K&Z CG3 6         | K&Z CG3 6         | K&Z CG3 6          |
| Averag. period (min)            | 1                     | 120                | 120                | 60                | 60                | 60                 |
| Start date of set               | 1 January 1995        | 1 January 1998     | 1 January 1998     | 28 August 2003    | 1 September 2003  | 1 September 2003   |
| End date of set                 | 31 December 2004      | 31 December 2001   | 31 December 2001   | 27 August 2007    | 31 August 2007    | 31 August 2007     |

<sup>a</sup> Annual avg. at 2 m level.

<sup>b</sup> Annual avg. at instr. level (approx. 2 m)

<sup>c</sup> Annual avg. at instr. level (approx. 6 m)

<sup>d</sup> K&Z = Kipp & Zonen.

Broeke *et al.*, 2004a, 2008), were selected for their continuous data sets of radiation, without data gaps caused by, e.g. sensor riming, frost accretion, snow accumulation, or instrument malfunctioning. The three Antarctic locations, Neumayer, AWS 5, and AWS 6 (Figure 1(a)), are located in Dronning Maud Land (East Antarctica) on the ice shelf, the coastal ice sheet and the escarpment region, respectively (Van den Broeke *et al.*, 2004a). The three Greenlandic stations (Figure 1(b)) are part of the Kangerlussuaq transect (K-transect), located at the western edge of the Greenland ice sheet (Van den Broeke *et al.*, 2008). Stations S5 and S6 are in the lower and middle ablation area, respectively, whereas S9 is located close to the equilibrium line.

At all AWS locations, Kipp & Zonen (K&Z) CNR1 radiometers measure all the radiation fluxes. A CNR1 houses four instruments: two CM3 pyranometers measure the incoming and reflected shortwave radiation,  $SW_{\downarrow}$  and  $SW_{\uparrow}$ , and two CG3 pyrgeometers measure downwelling and upwelling longwave radiation,  $LW_{\downarrow}$  and  $LW_{\uparrow}$ . At Neumayer, K&Z CM11 pyranometers and Eppley PIR pyrgeometers are used. Hourly averages are analysed in this study, apart from AWS 5 and 6 where 2-hourly data are used.

Energy considerations make ventilation of the AWS pyranometers unfeasible—but a steady katabatic flow of undersaturated air prevents riming of the sensors (Van den Broeke *et al.*, 2004b). Some corrections, such as for sensor tilt, have been applied to the radiation data (Van den Broeke *et al.*, 2004a, 2004b, 2008).

## 2.2. Cloud optical thickness ( $\tau$ )

The amount of shortwave radiation arriving at the surface,  $SW_{\downarrow}$ , is lower than the amount of downward shortwave radiation at the top of atmosphere (TOA),  $SW_{\downarrow,TOA}$ , due to scattering and absorption of radiation by the atmosphere and by clouds. In order to isolate the scattering and absorption due to clouds from clear-sky scattering and absorption, we use the cloud transmission,  $trc$ , which is the ratio of shortwave incoming radiation at the surface in the presence of clouds,  $SW_{\downarrow}$ , to the amount of radiation that would arrive at the surface without clouds,  $SW_{\downarrow,cs}$

$$trc = \frac{SW_{\downarrow}}{SW_{\downarrow,cs}} \quad (1)$$

This should not be confused with atmospheric transmission, which is the ratio of  $SW_{\downarrow}$  to  $SW_{\downarrow,TOA}$ .

For the calculation of  $trc$ , a value for clear-sky shortwave radiation,  $SW_{\downarrow,cs}$ , is required. For that, we follow the method of Greuell *et al.* (1997), who used expressions from Meyers and Dale (1983). This method relates  $SW_{\downarrow}$  to a series of transmission coefficients that account for Rayleigh scattering, and absorption by water vapour, other molecular gases, and aerosols. The transmission coefficient for aerosol absorption is used to tune the calculated  $SW_{\downarrow,cs}$  to measured values of  $SW_{\downarrow}$  for a clear sky. An example of the result of this procedure is shown in Figure 2 for S9 data. The curve for  $SW_{\downarrow,cs}$  fits as an envelope around the measurements of  $SW_{\downarrow}$ . Data from other stations are not shown but give similar results.

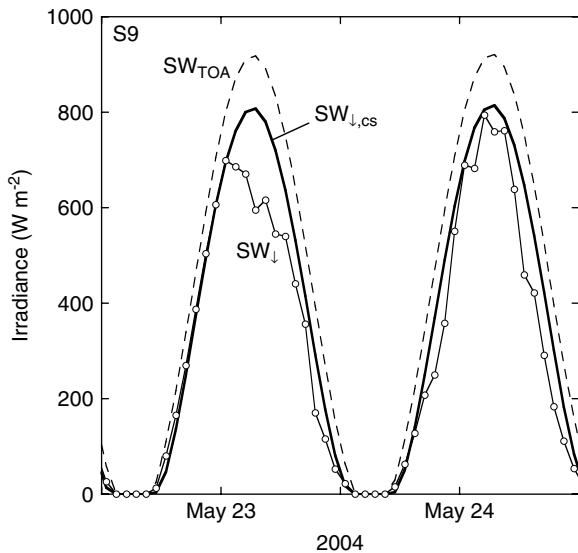


Figure 2. Hourly averages of  $SW_{\downarrow,TOA}$  and  $SW_{\downarrow}$  at S9 at two random days in 2004. The maximum incoming radiation at the surface,  $SW_{\downarrow,cs}$ , is calculated as explained in section 2.2.

When characterizing the effect of clouds on the surface shortwave radiation budget, it is important to describe the clouds with a quantity that is not dependent on the radiation field itself. In several previous studies (Konzelmann *et al.*, 1994; Bintanja and van den Broeke, 1996), cloud transmission, as defined in Equation (1), has been used to characterize the optical properties of the cloud. But, as pointed out by, e.g. Shine (1984) and Fitzpatrick *et al.* (2004), cloud transmission is strongly dependent on the zenith angle of the radiation (determining the path length of radiation through the cloud) and on the albedo of the surface: a high surface albedo gives rise to multiple reflections of radiation between the surface and the cloud base. The quantity  $trc$  is therefore not inherent to the cloud. A quantity that is inherent to the cloud is the cloud optical thickness,  $\tau$ . Fitzpatrick *et al.* (2004) successfully developed a parameterization for  $trc$  that depends on  $\tau$ , the broadband surface albedo,  $\alpha$ , and the solar zenith angle,  $\theta_0$ :

$$trc = \frac{a(\tau) + b(\tau) \cos \theta_0}{1 + (c - d\alpha)\tau} \quad (2)$$

where  $a$  and  $b$  are functions of  $\tau$ , and  $c$  and  $d$  are constants. The form of Equation (2) is based on theoretical considerations, and the values of the parameters have been derived by fitting Equation (2) to more than 500 computations done with a spectral multiple-scattering radiative transfer model where clouds are prescribed in terms of a cloud droplet distribution and an optical thickness. As a lower boundary condition for atmospheric radiative transfer, spectral albedo curves of sea-ice and snow surfaces are prescribed. In order to obtain hourly values of  $\tau$ , we use observed hourly values of  $trc$  (from Equation (1)) and  $\theta_0$ . Next, we search for a value of  $\tau$  that satisfies Equation (2). This retrieved value for  $\tau$  is unique since  $trc$  is a monotonically decreasing function of  $\tau$  for  $\tau \geq 0$ . Lastly, we calculate daily averages of

$\tau$  when more than 12 hourly values with  $\theta_0 < 85^\circ$  are available.

As instantaneous values of  $\alpha$  from CNR1 measurements are susceptible to large errors, hourly albedo values are obtained using the accumulated-albedo technique (Van den Broeke *et al.*, 2004b), in summary consisting of taking a 24 h running average albedo and superimposing a cloud-cover dependent daily cycle. This significantly reduces the error in  $\alpha$ .

The radiative properties of clouds depend on the cloud microphysics, represented by a cloud droplet distribution. It does not matter that the actual cloud droplet distribution is unknown, since Fitzpatrick *et al.* (2004) achieved a good fit between the radiative transfer model and the parameterization for several cloud droplet distributions. We use the values for  $a$ ,  $b$ ,  $c$ , and  $d$  that belong to an equivalent homogeneous clouds with an effective droplet radius of 8.6  $\mu\text{m}$ , as given by Fitzpatrick *et al.* (2004). As we do not have information on actual cloud microphysical parameters, the  $\tau$  in this paper characterizes the transmission of shortwave radiation and should not be used to infer cloud microphysical properties.

Fitzpatrick *et al.* (2004) argue that their parameterization is valid for both water and ice clouds, and that their parameterization is valid for a wide range of cloud droplet size distributions. Moreover, the parameterization is insensitive to the exact height of the cloud, and to the vertical distribution of cloud droplet size. This makes the parameterization suitable for a wide range of cloud types, including low Arctic stratus and high cirrus clouds, without the need to discriminate between different cloud types.

### 2.3. Longwave-equivalent cloudiness ( $N_\varepsilon$ )

The longwave radiation balance measured by an AWS can also be used to obtain a consistent and physically meaningful measure for cloud cover, which we will call 'longwave-equivalent cloudiness',  $N_\varepsilon$  (Van den Broeke *et al.*, 2004b).

#### 2.3.1. Obtaining $N_\varepsilon$

Longwave-equivalent cloudiness is based on differences in emissivity of a clear atmosphere and a cloudy one. Hourly values of downwelling longwave radiation  $LW_{\downarrow}$  are plotted against 2-m air temperature  $T_{2m}$  for the entire data set of each location (Figure 3). The upper bound of the scatter plot coincides with  $LW_{\downarrow} = \sigma T_{2m}^4$  (with  $\sigma = 5.67 \times 10^{-8} \text{ W m}^{-2} \text{ K}^{-4}$ , the Stefan–Boltzmann constant) and represents an entirely cloudy sky emitting as a blackbody radiator (emissivity  $\varepsilon \approx 1$ ). The lower bound of the scatter plot, which can be approximated by a second-order polynomial, represents clear-sky conditions, characterized by the lowest possible atmospheric emissivities. The polynomial is fitted to the 5th percentile of the data binned in 1 K intervals of  $T_{2m}$  (Van den Broeke *et al.*, 2004b). Some data points (2–3% of the total number) end up below the lower, clear-sky bound and are considered clear-sky cases. Linearly interpolating

between these bounds yields a value for  $N_\varepsilon$  between 0 and 1. From the hourly values, daily averages are calculated, which are used in a regression with  $\tau$  in section 3.

The lower bound in Figure 3 is described by a polynomial rather than using a constant clear-sky emissivity, because in polar regions, surface inversions occur frequently, particularly during clear-sky conditions at nighttime and in winter, which makes surface temperature less representative for the vertical temperature structure. A constant emissivity for clear-sky conditions would therefore not hold.

### 2.3.2. $N_\varepsilon$ and cloud type

It should be stressed that the longwave-equivalent cloudiness ( $N_\varepsilon$ ) is not a cloud cover or cloudiness in the usual meteorological sense ( $N$ ), expressed in eighths (octas) or tenths, which is based on visual observation. For example, both a fully high cirrus-covered sky and a fully low stratus-covered one would correspond to  $N = 1$ . However, as high cirrus clouds have a much smaller impact on  $LW_\downarrow$  at the Earth's surface than low stratus clouds (e.g. Dürr and Philipona, 2004), the value for  $N_\varepsilon$  of the fully cirrus-covered sky would be much lower than of the fully stratus-covered one. In other words,  $N_\varepsilon$  is closely tied to sky emissivity and thus to the net longwave cloud forcing, rather than to the fraction of the sky covered by clouds.

## 3. Results

In this section, we will apply the methods from the previous section to the AWS data sets described before. We will show that there is a correlation between  $N_\varepsilon$  and  $\tau$ , which allows for the calculation of cloud optical thickness

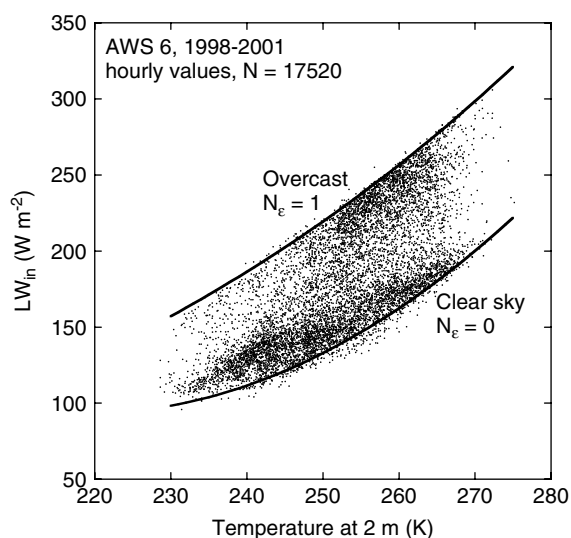


Figure 3. Scatter plot of air temperature at 2 m against downwelling longwave radiation  $LW_\downarrow$ , for hourly data of AWS 6, Antarctica. The upper bound coincides with  $LW_\downarrow = \sigma T_{2m}^4$ , the lower bound is a fitted polynomial of second degree. Longwave-equivalent cloudiness  $N_\varepsilon$  is obtained by linearly interpolating between the two bounds for a given  $T_{2m}$ .

throughout the year for all locations. Uncertainties in this procedure will be discussed.

### 3.1. Correlating $N_\varepsilon$ and $\tau$

In an independent way, both the longwave and the shortwave radiation balances yield objective measures for cloud cover. These can be expected to correlate, since a low value for  $\tau$  should imply a low value for  $N_\varepsilon$ , and a high  $\tau$  should coincide with a high  $N_\varepsilon$  as well. Figure 4(a)–(f) shows scatter plots of  $\tau$  against  $N_\varepsilon$  at all locations, for all daily-averaged values of  $\theta_0 < 80^\circ$ . Least-squares regressions of the form

$$\tau = c_1(e^{c_2 N_\varepsilon} - 1) \quad (3)$$

show a correlation coefficient  $r$  between 0.77 and 0.94 (shown in the upper-left corners of Figure 4(a)–(f) as well as in Table II; values of  $c_1$  and  $c_2$  are also given in Table II). Although there is no clear physical argument, the form of Equation (3) is chosen as it intersects the origin, is monotonically increasing and uses a minimum of fit coefficients while still exhibiting the exponential behaviour seen in the observations.

The correlation is second-highest for Neumayer, the station with the longest data series and the highest quality of measurements. Furthermore, the correlation is on average lower for the Greenland stations than for the Antarctic stations, since shortwave radiation measurements over melting surfaces inherently pose more problems with sensor tilt, thus impacting the retrieval of  $\tau$ . We will expand on this in section 3.3.

Table II. Coefficients used in Equation (2) to relate cloud optical thickness  $\tau$  to longwave-equivalent cloudiness  $N_\varepsilon$ . Correlation coefficient  $r$  is given in the rightmost column.

| Station  | $c_1$ | $c_2$ | $r$  |
|----------|-------|-------|------|
| Neumayer | 1.14  | 3.20  | 0.89 |
| AWS 5    | 1.87  | 2.73  | 0.89 |
| AWS 6    | 0.93  | 3.68  | 0.94 |
| S5       | 2.09  | 2.58  | 0.82 |
| S6       | 2.80  | 2.12  | 0.77 |
| S9       | 1.38  | 2.77  | 0.85 |

Table III. Characteristics of the narrowband sensors used in Figure 10 to illustrate spectral albedo effects under clear and cloudy sky for snow and ice surfaces. MODIS = Moderate Resolution Imaging Spectroradiometer, MISR = Multiangle Imaging Spectroradiometer, AVHRR = Advanced Very High Resolution Radiometer.

| Instrument | Band | Wavelength range (nm) | Central wavelength (nm) |
|------------|------|-----------------------|-------------------------|
| AVHRR      | 1    | 574–704               | 639                     |
| MISR       | 3    | 663–679               | 671                     |
| MODIS      | 2    | 838–875               | 857                     |

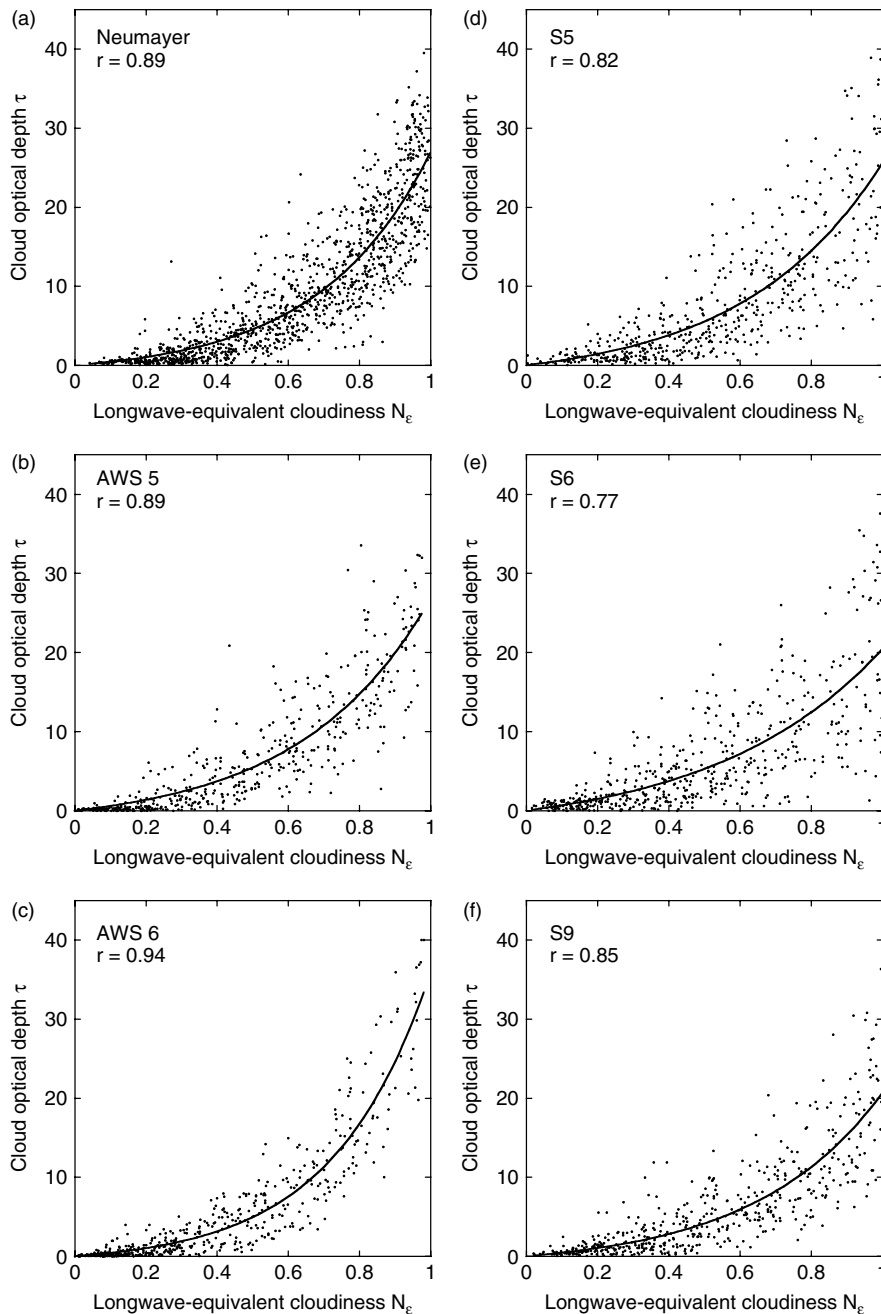


Figure 4. Longwave-equivalent cloudiness  $N_\epsilon$  against cloud optical thickness  $\tau$  for daily averages of (a) Neumayer (1995–2004), (b) AWS 5 (1998–2001), (c) AWS 6 (1998–2001), (d) S5 (2003–2007), (e) S6 (2003–2007), and (f) S9 (2003–2007). Least-squares regressions, using only days for which average  $\theta_0 < 80^\circ$ , are shown as the solid curves. The functional form of the fits is given in Equation (3). The correlation coefficient  $r$  for each fit with the data is given in the upper-left corner of each panel, as well as in Table II.

The good correlation between  $N_\epsilon$  and  $\tau$  provides a means to calculate optical properties of clouds even in absence of solar radiation (at night or in winter), as we will show further in this section. Year-round records of cloud characteristics may be useful in assessing the wintertime performance of numerical weather prediction models over ice sheets using AWS data.

### 3.2. Cloud climatology from observations

Cumulative probability distributions of summertime daily values of  $\tau$  in Greenland and Antarctica are shown

in Figure 5(a) and 5(b). Only data for which daily-averaged  $\theta_0 < 80^\circ$  are used (Greenland: typically mid-April to end of August, Antarctica: end of October to mid-February). In Greenland (Figure 5(b)), differences between the stations are small, since they are in relatively close proximity to each other (the distance between S5 and S9 is only 82 km). At S5,  $\tau > 10$  for 30% of the time, whereas at S6 and S9, this is 22 and 23%, respectively. The occurrence of optically very thick clouds ( $\tau > 20$ ) is lowest at S6 and S9 (<6%). The landward decrease in  $\tau$  is caused by a decrease of precipitable water at higher altitudes, thereby making clouds optically thinner.

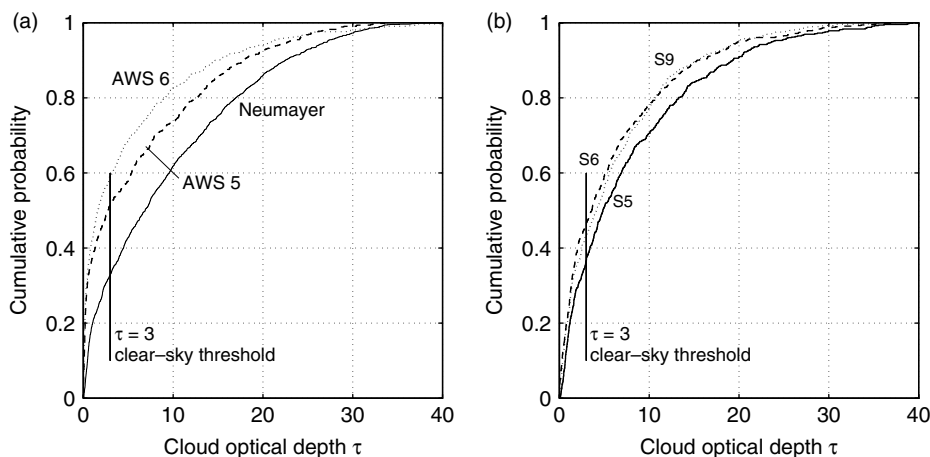


Figure 5. Cumulative probability distributions of daily-averaged cloud optical thickness  $\tau$  for all data where  $\theta_0 < 80^\circ$  for (a) all Antarctic stations and (b) all Greenland stations.

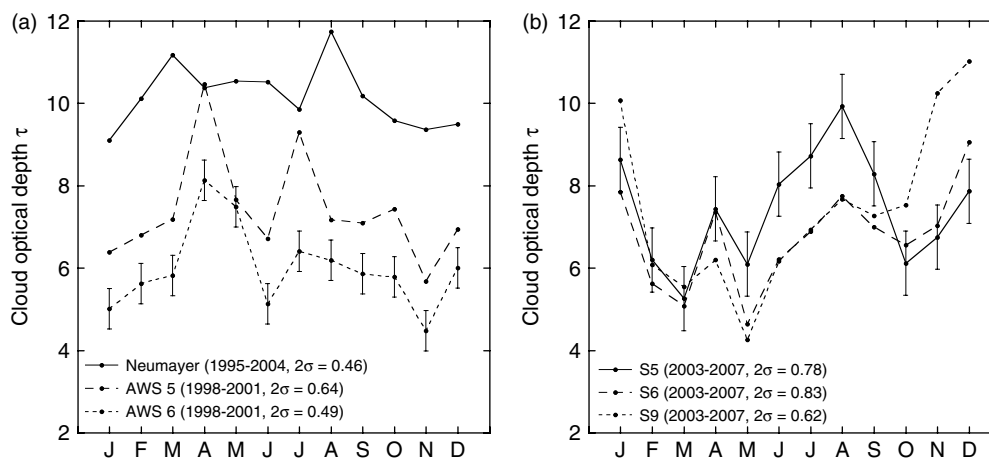


Figure 6. Monthly averages of  $\tau$  throughout the year for the entire data period, obtained from a regression with  $N_g$ ; for (a) Antarctica and (b) Greenland. The reported  $2\sigma$  values are derived from the RMSE values of the fits in Figure 4(a)–(f), and represent the 95% confidence interval for the monthly averages. Interannual variability is not shown but discussed in the text.

In Antarctica, differences are larger, partly due to the larger distances between the stations. AWS 6 stands out as by far the sunniest station, with the most clear-sky occurrence ( $\tau < 3$  for 59% of the time). At AWS 5, clear-sky occurrence amounts to 51%, while at Neumayer, it is 33%. Clouds at AWS 6 are also optically thinner than at AWS 5 and Neumayer. Values of  $\tau > 20$  occur most frequently at Neumayer (14% of the time), and less at AWS 5 (8%) and AWS 6 (6%). Again, a smaller precipitable water amount with increasing altitude can explain the optical thinning of clouds towards the interior.

Using the regression curves shown in Figure 4(a)–(f), we calculated monthly averages for  $\tau$  throughout the year for all locations (Figure 6). Figure 6(b) resembles figure 10 in Van den Broeke *et al.* (2008), and is shown here to update the values from that paper, originating from different fit functions. In Figure 6, the error bars for AWS 6 and S5, as well as the values in the figure legends, represent  $2\sigma$ -uncertainties due to the spread of data points around the fits in Figure 4, discussed in detail in section 3.3. At Neumayer (long data series), AWS

6 and S9 (good fits), the 95% confidence intervals are smallest (0.46, 0.49, and 0.64 resp.).

Comparison with  $\tau$  retrievals by Ricchiuzzi *et al.* (1995) over Palmer Station, Antarctica, reveals that the cumulative probability function of  $\tau$  at Palmer Station is very similar to those of Neumayer and AWS 5. Since these stations are all in coastal regions, the retrieved values of  $\tau$  seem reasonable. The range of  $\tau$ -values at the Antarctic coast contrasts strongly with values reported over the Antarctic interior at South Pole (Mahesh *et al.*, 2001), but the cloud climatology over the interior is very different, with fewer and optically thinner clouds, and a much smaller water vapour column.

At the locations in Greenland, an increase in  $\tau$  is apparent in the summer, between May and August (Van den Broeke *et al.*, 2008). This feature appears robust and concurrent at all locations. The same has been observed at Summit, Greenland (Hoch, 2005). It is likely that the increased water vapour budget in the atmosphere increases the average cloud cover, and therewith the monthly average  $\tau$ . So although melt at these locations

lowers the surface albedo and increases the net shortwave radiation budget, this increase is partially offset by an increasing optical thickness of the cloud cover. Monthly averages of cloud fraction at the nearby locations DYE 2 and DYE 3 clearly show the same pattern of an increased cloud cover throughout summer (Griggs and Bamber, 2008).

At the Antarctic stations,  $\tau$  also increases at all stations in the summer months (November–March), although this finding is less robust than over Greenland as it is not observed consistently for every year.

The interannual variability of  $\tau$  is high at all stations, but the AWS data records are too short to present meaningful statistics. The increase of  $\tau$  in Greenland in the summer months is, however, a yearly recurrent feature. Only the 10-year Neumayer data series are of sufficient length to give insight on the magnitude of the interannual variability. Standard deviations from the mean of the detrended 10-year Neumayer data set of  $\tau$  range from 1.6 (March) to 2.7 (October) with an average of 2.1.

### 3.3. Uncertainties

In the retrieval of  $\tau$  using Equation 2, the errors in  $\tau$  are determined by (1) errors in  $trc$ ; (2) errors in  $\alpha$ ; and (3) the use of a constant cloud droplet size and distribution in the method by Fitzpatrick *et al.* (2004) for the retrieval of  $\tau$ . Additionally, when using  $N_\varepsilon$  to infer  $\tau$ , the accuracy of longwave radiation measurements also impact the uncertainty of  $\tau$ . Below, we will discuss each of these sources of uncertainty. Using the data series of location S6, we compute the cumulative effect of all individual errors on the uncertainty in  $\tau$  and  $N_\varepsilon$ .

#### 3.3.1. Uncertainties in $trc$

Two sources contribute to errors in  $trc$ : uncertainties in the measurement of  $SW_\downarrow$  by the pyranometer, and the fitting of the  $SW_{\downarrow,cs}$ -curve to the  $SW_\downarrow$  data. Instantaneous  $SW_\downarrow$  measurements using an unventilated, field-calibrated CNR1 pyranometer are subject to errors of typically 8.4% for hourly measurements (Michel *et al.*, 2008). By omitting high- $\theta_0$  data, for which the CNR1 performance is poor, Van den Broeke *et al.* (2004b) found smaller rms errors in the hourly data of 4–5%. As for some locations, the correction for possible instrument tilt adds some uncertainty, we take the upper limits of this range (5%) for hourly data. A misfit of  $SW_{\downarrow,cs}$  to the  $SW_\downarrow$  data of 2% is immediately detected by eye in the fitting process, leaving the overall uncertainty in hourly values of  $trc$  at 5%.

#### 3.3.2. Uncertainties in $\alpha$

Rather than taking pairs of instantaneous values of  $SW_\downarrow$  and  $SW_\uparrow$  for calculating  $\alpha$ , we make use of the accumulated-albedo technique (Van den Broeke *et al.*, 2004b), which dramatically reduces the uncertainty of hourly values. In brief, this method consists of computing

a 24-h running average of albedo using 24-h accumulated shortwave fluxes. To restore the daily cycle in albedo, a theoretical daily cycle, depending on the diffuse fraction (estimated with  $N_\varepsilon$ ) is superimposed. We ascribe an error of 3% to hourly values of  $\alpha$ .

#### 3.3.3. Uncertainties in cloud droplet distribution

The third source of uncertainty in the retrieval of  $\tau$  comes from the assumption in the method by Fitzpatrick *et al.* (2004) that the cloud droplet distribution of all clouds is the same. As explained above, Fitzpatrick *et al.* (2004) show that a good parameterization of  $\tau$  can be obtained using several cloud droplet distributions, but each parameterization will lead to slightly different values for  $\tau$ . In Figure 7, we show these differences for station S5. The values for  $\tau$  that we obtained with the default cloud droplet distribution, with an effective cloud droplet radius  $r_e = 8.6$   $\mu\text{m}$ , are binned in intervals of  $\Delta\tau_{8.6} = 5$ . The average  $\tau_{8.6}$  in each bin is then compared to the average  $\tau_{6.0}$  and  $\tau_{20.0}$ . For large  $\tau_{8.6}$ , values of  $\tau_{20.0}$  deviate most from  $\tau_{8.6}$ , the average  $\tau_{20.0}$  being 3.5 larger (11%). The largest relative difference is in the clear-sky bin ( $0 < \tau_{8.6} < 2$ ), where  $\bar{\tau}_{8.6} = 0.64$  and  $\bar{\tau}_{20.0} = 1.17$ , meaning that the amount of clear-sky data becomes somewhat dependent on the choice of the parameterization for  $\tau$ .

#### 3.3.4. Combined uncertainties for $\tau$

The combined uncertainty for  $\tau$  due to the above sources of error cannot be derived by analytical means. Instead, we perturb the original hourly data series of both  $trc$  and  $\alpha$  with random errors drawn from a normal distribution. The normal distribution from which the error for  $trc$  is drawn has a standard deviation equal to the error assigned in section 3.3.1. The same is done for the error in  $\alpha$  using errors assigned in section 3.3.2. Furthermore, we randomly alternate the cloud droplet distribution. Using station S6 as an example, the impact of these errors is discussed as rms differences between the original and perturbed data series, for hourly, daily, and monthly means.

For hourly data, the rms difference between the original and perturbed data series is 1.4. Considering that the average of hourly values of  $\tau$  is 6.8, this rms difference is rather large (21%). For daily means, the rms differences is reduced to 0.7 (11% of the average daily  $\tau$  of 6.3). If we only consider  $\tau < 10$  data, the rms differences are 0.83 for hourly values, and 0.46 (14% of average daily value of the  $\tau < 10$  subset) for daily means. For  $\tau > 20$  data, hourly values have rms differences of 2.7 (9% of average hourly value for the  $\tau > 20$  subset), and that of daily means is 1.2 (4%). The rms differences for daily means are smaller than those for hourly means, and the performance of the method for daily values is better. In relative terms, we can conclude that the uncertainty decreases as  $\tau$  increases. Finally, the rms difference for monthly means is 0.48, indicating that the method is

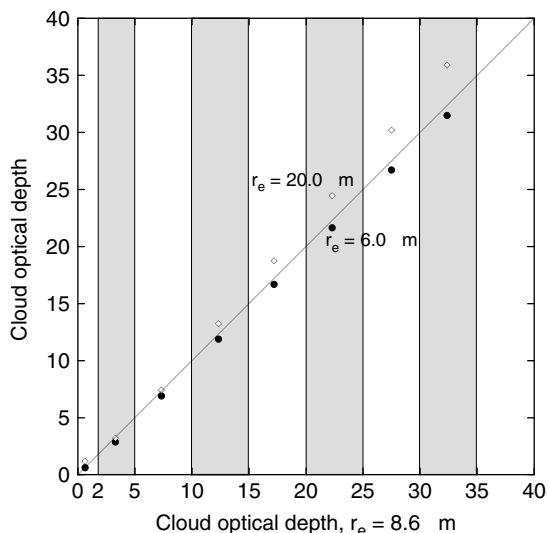


Figure 7. Uncertainty in retrieved  $\tau$  at S5 due to assuming a constant droplet size distribution (with effective droplet radius  $r_e$ ) in the parameterization of  $\tau$  by Fitzpatrick *et al.* (2004). The average  $\tau$  is plotted for each bin of 5 for the  $r_e = 6.0$  m (black dots) and 20.0 m (open diamonds) distributions, against the default  $r_e = 8.6$  m distribution. The 0–5 bin has been separated into a 0–2 and a 2–5 bin.

suitable to determine monthly means of  $\tau$  with a relative error of about 6%.

The errors found for S6 are representative for all locations, except for Neumayer, where higher-quality pyranometers are used. The errors in  $\tau$  for Neumayer are expected to be lower, as the errors in  $\text{trc}$  and  $\alpha$  are lower.

A remaining uncertainty that is difficult to quantify, is related to the fact that the values of the coefficients in Equation (2) are fitted only to data for which  $\alpha \leq 0.83$  (Fitzpatrick *et al.*, 2004). It is therefore conceivable that both a random and a structural error occurs in  $\tau$ -retrievals when albedo rises much above 0.83. For higher  $\alpha$ , which occur frequently especially at Antarctic locations, the computation of  $\tau$  becomes more sensitive to the uncertainty in  $\alpha$ . It is therefore likely that this additional source of random error increases the stated errors for the retrieval of  $\tau$  for very high albedos. Moreover, as the parameterization is fitted to data for which  $\alpha \leq 0.83$ , a structural upward or downward bias may be introduced when applying the parameterization to higher-albedo data. Further research is required to pin down this contribution quantitatively.

### 3.3.5. Uncertainties in $N_\epsilon$

The accuracy of the fit is also influenced by uncertainties in  $N_\epsilon$ , caused both by measurement errors of  $LW_\downarrow$  and by the determination of  $N_\epsilon$  (section 2.3.1).

The method to determine  $N_\epsilon$  from  $LW_\downarrow$  (section 2.3.1) is sensitive only to random errors in  $LW_\downarrow$ , not to offset errors. Errors in  $LW_\downarrow$  will therefore be smaller than 5–6% reported by Van den Broeke *et al.* (2004b), who found that measurement errors are mainly offset errors and that the random error is small. We assume a random

error of 2%. The fit procedure to obtain the clear-sky lower limit of  $N_\epsilon = 0$  may add an additional 2% of uncertainty. By assigning normally-distributed random errors to the lower bound of  $LW_\downarrow$  and to  $LW_\downarrow$  itself, we find that the error for hourly values of  $N_\epsilon$  is 0.047. For daily values of  $N_\epsilon$ , this reduces to 0.011. The latter translates to an additional uncertainty when translating  $N_\epsilon$  to  $\tau$  using the fits in Figure 4. This will be discussed in the next section.

### 3.3.6. Uncertainties in the $\tau(N_\epsilon)$ fit

The spread around the fits in Figure 4(a)–(f) leads to an uncertainty in the retrieval of  $\tau$  from  $N_\epsilon$ . As the residuals of each fit are approximately normally distributed around the fit, the standard deviation of the daily values was used to calculate 95% confidence intervals ( $2\sigma$ ) of the monthly means in Figure 6 (error bars and values in figure legends). We here used the fact that, if the standard deviation of the daily values is  $\sigma_d$ , the standard deviation of a monthly average from multiple years is  $\sigma_d/\sqrt{YD}$ , where  $D$  is the number of days in a month, and  $Y$  the number of years considered.

An additional uncertainty in the  $\tau(N_\epsilon)$  retrieval is caused by the uncertainty in  $N_\epsilon$  (section 3.3.5). For daily values, the 0.011 uncertainty in  $N_\epsilon$  translates to a 0.22 error in daily values of  $\tau$ . Compared to the uncertainty caused by the spread around the fits in Figure 4, this is a negligible amount. In the remainder of this paper (section 4), we will therefore disregard this source of error.

The spread around the fits suggests that a range of cloud optical thickness can be found for one value of  $N_\epsilon$ . The other way around, one value of  $\tau$  can occur for a range of values for  $N_\epsilon$ . It indicates that the assumption that a certain cloud uniquely determines both the longwave and shortwave radiation budgets is violated to a certain extent. A part of the spread is probably related to the occurrence of different cloud types. In general, high cirrus clouds have a low impact on  $LW_\downarrow$ , leading to low values of  $N_\epsilon$ . At the same time, high cirrus has a low  $\tau$  as incoming solar radiation is only weakly decreased (Duchon and O’Malley, 1999). Events with high cirrus clouds thus tend to become clustered in the low- $\tau$ –low- $N_\epsilon$  regions of Figure 4(a)–(f). Low stratus clouds, profoundly impacting both the longwave and shortwave budgets at the surface, will constitute the broad tail of the fits in the high- $\tau$ –high- $N_\epsilon$  regions. Even when ignoring the fact that different cloud types occur on one location, still good correlations between  $\tau$  and  $N_\epsilon$  are obtained, which adds to the strength of the method.

## 4. Applications

The inferred values of  $\tau$  can be used to distinguish between clear and cloudy days. From the daily averages of  $\tau$ , we have extracted a subset of clear days ( $\tau < 3$ ) and a subset of fully overcast days ( $\tau > 14$ ). To test the clear-sky threshold of  $\tau = 3$ , we applied the Marty

and Philipona (2000) method to construct alternative clear-sky data sets, and found out that the average  $\tau$  of those data sets was 2.3, suggesting that a maximum value of 3 is a reasonably strict criterium compared to existing methods. As three applications of the method presented above, we discuss the influence of clouds on the radiation budget (Application I), the relation between cloud cover and broadband albedo (Application II) at the six AWS locations, and we demonstrate the possibility to detect trends in  $\tau$  in longer data series (Application III). Applications I and II merely show how additional valuable information can be obtained by separating a data series into clear and overcast subsets using the method outlined above. Application III demonstrates that long, robust, and consistent time series of cloud optical thickness can be obtained using the method.

#### 4.1. Application I: Clouds and multiple reflections

Clouds shield the surface from solar radiation by reflecting it back to space, and by absorption. Over highly reflective surfaces however, a cloud will compensate a part of this loss of solar radiation through the effect of multiple reflection between the surface and the cloud base. As an application, the magnitude of this effect can be calculated simply by inserting  $\alpha = 0$  into Equation (2), so that multiple reflections by clouds are ignored. The incoming radiation with and without multiple reflection is plotted for station S6 in Figure 8 as an example. For the cloudy data sets, the effect enhances  $SW_{\downarrow}$  by more than a factor of 2 in May and decreases to a factor of 1.5 from July onwards when the ice surface appears.

The enhancement is thus strongest at locations with a high albedo and frequent cloud cover. Averaged over all summer days, multiple reflection enhances the monthly incoming flux strongest at Neumayer (29%). The effect is weakest at S5 (18%) in Greenland due to lower surface albedos of ice in summer. At S6, shown in Figure 8, the incoming flux is enhanced by 25%. The effect of a

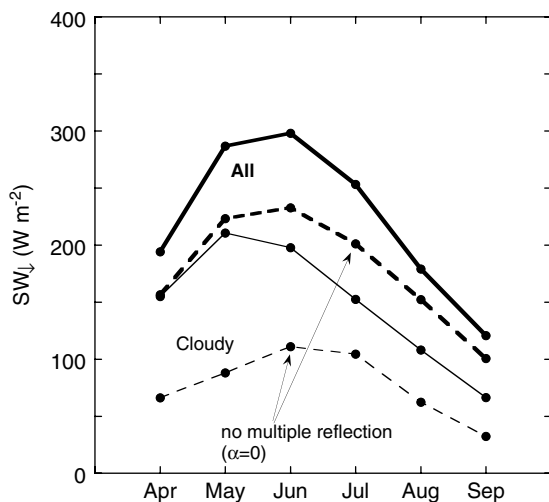


Figure 8. Incoming shortwave radiation at S6 (monthly averages) for cloudy days (thin lines) and all days (thick lines). Dashed lines are without multiple reflections between surface and cloud base.

particular cloud on  $SW_{\text{net}}$  is thus strongly reduced as it moves from a low-albedo surface (like the ocean) over a high-albedo snow or ice surface, even if the cloud does not change physically.

#### 4.2. Application II: Clouds and albedo

Another application in which  $\tau$  is used to separately analyse clear and overcast conditions is the assessment of cloud effects on surface albedo.

Clouds alter the broadband albedo of a snow surface mainly by filtering out radiation at near-infrared (IR) wavelengths ( $>800$  nm) more effectively than radiation in the visible region: the spectral composition of the radiation arriving at the surface changes. As the spectral albedo for visible wavelengths is higher than for near-IR wavelengths, the spectrally-integrated albedo increases. This 'spectral effect' is amplified by multiple reflections between the surface and the cloud base: after each reflection, the radiation gets more depleted in near-IR wavelengths (Wiscombe and Warren, 1980).

Another effect of clouds is that most of the solar radiation arriving at the snow surface is diffuse under an overcast sky. For spectral albedo, diffuse radiation has an effective solar zenith angle  $\theta_0$  of about 50 (Wiscombe and Warren, 1980). As spectral albedo increases for higher  $\theta_0$ , clouds tend to decrease spectral albedo when  $\theta_0 > 50$ . This 'diffuse radiation effect' is clearly seen for spectral albedo, but for broadband albedo, the 'spectral effect' outlined above dominates by far over snow surfaces.

Daily-averaged albedos are plotted for all stations in Figure 9(a)–(f). At all stations, the clear-sky albedo,  $\alpha_{\text{cs}}$ , varies throughout the year. In Greenland, the most important cause for these variations is snow melt and the subsequent appearance of the ice surface. But even in Antarctica, there is significant clear-sky albedo variation (0.75–0.85), which was shown by Kuipers Munneke *et al.* (2008) to be primarily due to snow metamorphism, and to a lesser extent by the seasonal cycle in  $\theta_0$ . At all Antarctic stations (Figure 9(a)–(c)), the albedo under cloudy sky,  $\alpha_{\text{cl}}$ , is larger than  $\alpha_{\text{cs}}$  throughout the summer, due to the dominating spectral effect. From the Greenland data, a more complicated picture emerges: at S9, situated at the equilibrium line altitude,  $\alpha_{\text{cs}}$  decreases gradually throughout the season until late August, when the superimposed ice horizon surfaces for one to a few weeks. In 2007, the winter snow cover already disappeared in June, seen as a cluster of low- $\alpha_{\text{cs}}$  data in the box in Figure 9(f). Generally, clouds enhance broadband albedo throughout the summer at S9. The same is true for the high-albedo spring snow surface at S6, until the snow has melted away and the ice appears. From then on,  $\alpha_{\text{cs}}$  and  $\alpha_{\text{cl}}$  are no longer discernible (Figure 9(d)–(e)). At S5, there is almost no snow accumulation, and before the 1st of June, there is intermittent snow cover. A consistent feature is that the distinction between  $\alpha_{\text{cs}}$  and  $\alpha_{\text{cl}}$  disappears when snow cover has completely melted away (which is recorded

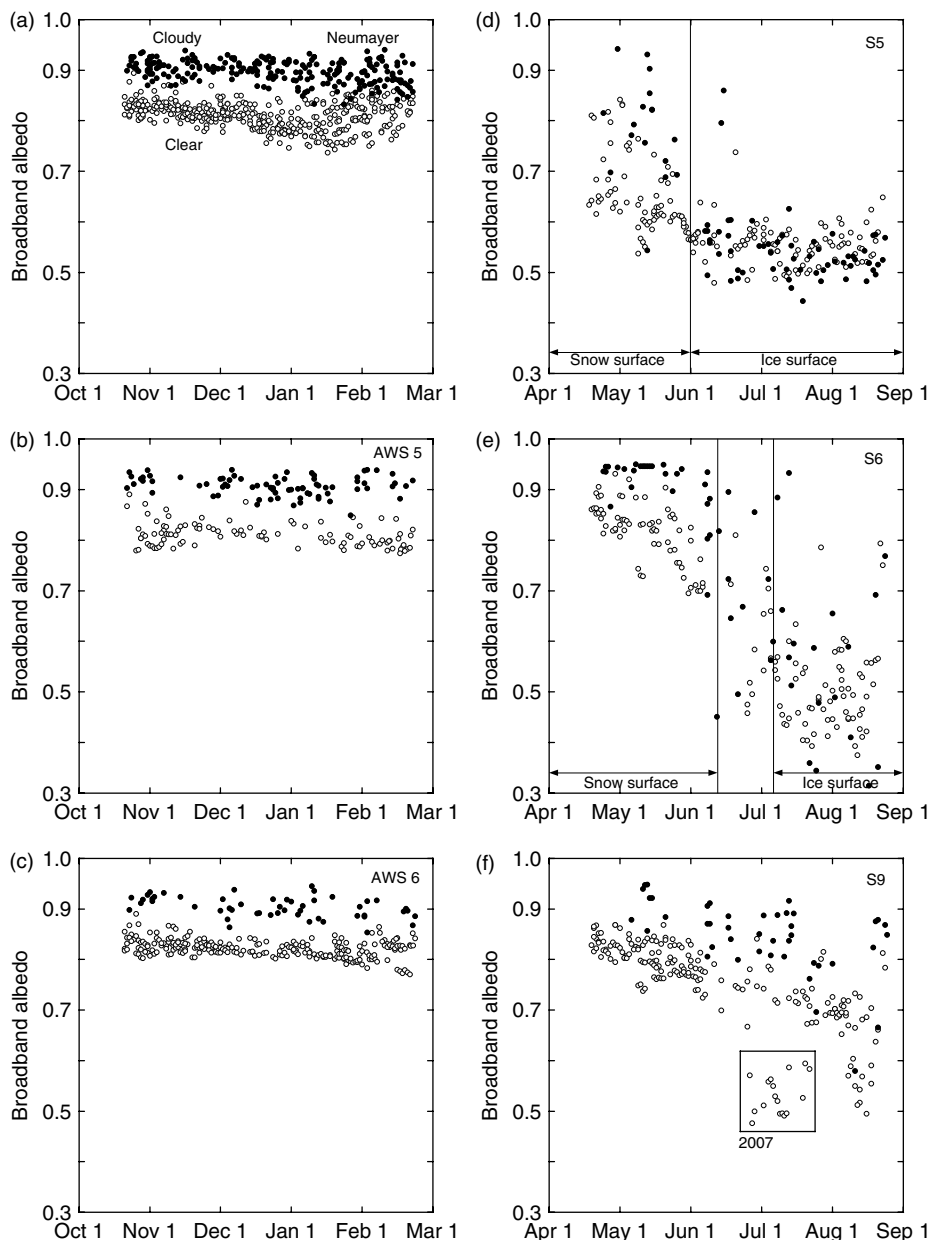


Figure 9. Daily averages of broadband albedo for clear (open dots) and cloudy (solid dots) days at (a) Neumayer (1995–2004), (b) AWS 5 (1998–2001), (c) AWS 6 (1998–2001), (d) S5 (2003–2007), (e) S6 (2003–2007), and (f) S9 (2003–2007).

by a sonic height ranger for measuring snow depth). At S5, this was consistently around the 1st of June for the considered period, whereas at S6, this happens somewhere between mid-June and the beginning of July.

Three narrowband pyranometers (Knap *et al.*, 1999; Greuell and Oerlemans, 2004) that operated at S6 in 2004–2005 are used to explain why  $\alpha_{cs}$  and  $\alpha_{cl}$  become indiscernible over ice (see Table III for characteristics of these narrowband pyranometers). Two pairs of days were selected: 15 (cloudy) and 17 (clear) May 2005 both had a snow cover at S6, while at the 2nd (clear) and 5th (cloudy) of August, ice was at the surface. Narrowband albedo from these pyranometers are presented in Figure 10 for these days.

For the snow cover (15 and 17 May), spectral albedo under clouds is only a bit lower than under a clear-sky,

in line with the ‘diffuse radiation effect’ (Wiscombe and Warren, 1980). The narrowband measurements agree well with theoretical spectral albedo curves obtained by applying the Wiscombe and Warren (1980) model with a snow grain radius of 800  $\mu$ m. The directly measured broadband albedo under clouds (0.86) is much higher than for the clear sky (0.73), in accordance with the ‘spectral effect’ as discussed above.

For the ice surface (2 and 5 August), clear-sky narrowband albedos are about 0.10 higher for visible shortwave radiation than albedo under a cloudy sky. This difference is possibly due to different surface conditions. This time however, the directly measured clear-sky broadband albedo (0.47) is only slightly higher than the albedo under clouds (0.44). The reason is that spectral albedo for ice is only 0.4–0.6 in the visible region, so that

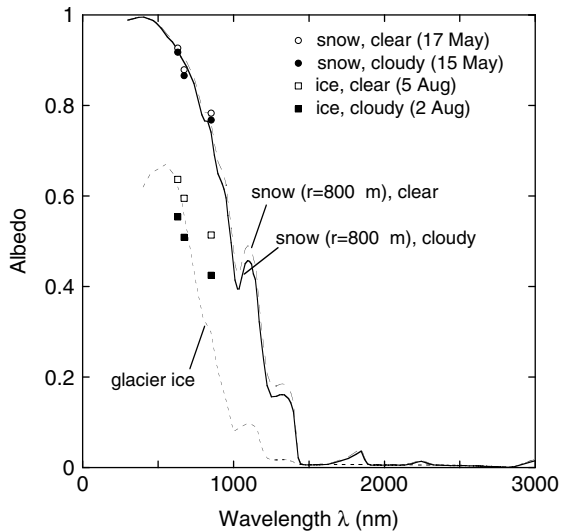


Figure 10. Narrowband albedos at S6 on a clear (open symbols) and cloudy day (closed symbols) for a snow (circles) and an ice (squares) surface. The solid and the adjacent dashed lines are theoretical snow albedos for a grain size of 800  $\mu\text{m}$  (calculated using Mie scattering), and the separate dashed line is for glacier ice albedo taken from Zeng *et al.* (1984), extended beyond 1150 nm with calculations from very large snow grains ( $>3 \mu\text{m}$ ).

multiple reflection between surface and cloud is much weaker than for snow. The enrichment of visible radiation that is important for the ‘spectral effect’ ceases to enhance broadband albedo. Even when the observed narrowband albedos are quite different in the visible, the broadband albedo changes hardly. For reference, we plotted the albedo curve for glacier ice by Zeng *et al.* (1984) in Figure 10.

By comparing clear-sky and cloudy-sky albedo over a snow and an ice surface, we can conclude that over snow surfaces, the spectral albedo changes only slightly due to the ‘diffuse radiation effect’, whereas the broadband albedo increases dramatically under an overcast sky due to the ‘spectral effect’. For an ice surface however, the

observed narrowband albedo may vary a lot (about 0.10 in Figure 10) but the effect on broadband albedo is very small.

The decrease in visible enrichment also explains observations by Brock *et al.* (2000) at Glacier Haut d’Arolla, Switzerland, and those by Jonsell *et al.* (2003) at Storgläciären, Sweden. Brock *et al.* (2000) found no correlation between ice albedo and  $\theta_0$  or cloud cover. Jonsell *et al.* (2003) also observed only a very weak albedo change under cloudy skies.

#### 4.3. Application III: Trends at Neumayer

Another useful application of the method is to detect long-term trends in cloud optical thickness from longer data series. The data series at Neumayer are sufficiently long for this purpose. In Figure 11, we show time series of  $\tau$  at Neumayer for the period 1995–2004. The uncertainty of each monthly value (shown in Figure 11 as the grey band around the graph) is due to the uncertainty in the  $\tau$ - $N_e$  fit (section 3.3.6), and to the uncertainty in  $\tau$  (section 3.3.4). There is a trend of  $-0.40 \pm 0.15 \text{ y}^{-1}$  (significant at the 95% confidence level), indicating that the radiation balance of the snowpack is gradually changing. This is in line with the observed trend in increasing incoming solar radiation of  $+1.24 \text{ W m}^{-2} \text{ y}^{-1}$  at Neumayer since the 1990s (Wild *et al.*, 2005). The causes of this increase in incoming surface shortwave radiation (and thus, a decrease in  $\tau$ ) are currently under debate, but it is beyond the scope of this article to discuss this any further. However, we do show that such trends in the cloud climate of snow- and ice-covered regions can be determined.

## 5. Conclusions

In this study, we have critically reviewed a method to obtain quantitative information on clouds from radiation measurements made with AWSs over snow and

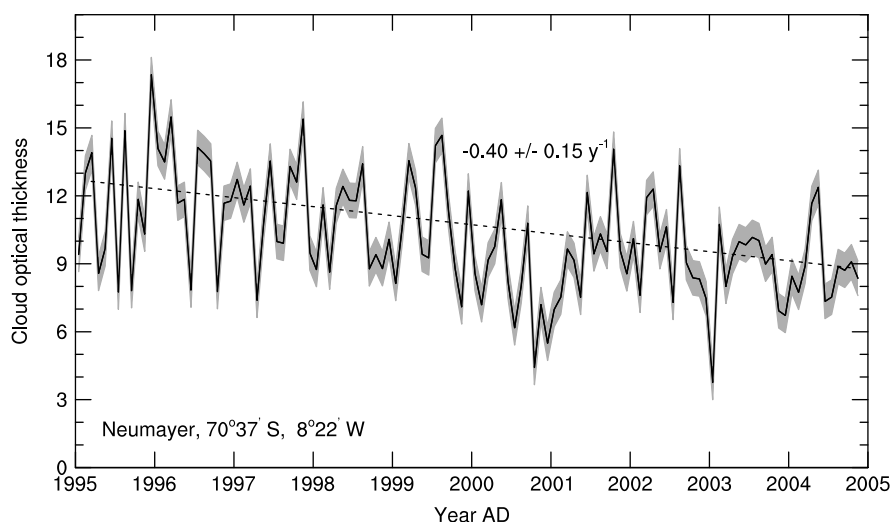


Figure 11. Monthly values of retrieved cloud optical thickness  $\tau$  between 1995 and 2004, at Neumayer, Antarctica. The dashed line shows the downward trend in  $\tau$  of  $-0.40 \text{ y}^{-1}$ .

ice surfaces (Van den Broeke *et al.*, 2008; Giesen *et al.*, 2009). The longwave radiation balance yields a 'longwave-equivalent cloudiness',  $N_\varepsilon$ , which is closely tied to the emissivity of the sky. For clear skies,  $N_\varepsilon = 0$  and for overcast skies,  $N_\varepsilon = 1$ . The shortwave radiation balance can be used to infer the cloud optical thickness,  $\tau$ , using the parameterization by Fitzpatrick *et al.* (2004).

Using data sets from six different climatic regions in Greenland and Antarctica, we have shown that the cloud optical thickness  $\tau$  correlates well with  $N_\varepsilon$ , which is determined entirely independently from the longwave radiation balance. This correlation for each location can be used to infer shortwave cloud properties even in the absence of solar radiation, an application which may be useful in the validation of weather and climate models over ice sheets during wintertime.

A correct retrieval of  $\tau$  is sensitive to errors in the input data ( $\text{trc}$  and  $\alpha$ ), as well as to the fact that the cloud droplet distribution of the overlying clouds is unknown. Instantaneous hourly values of  $\tau$  are subject to a relative error of about 21%, although the relative error decreases when only taking optically thicker clouds into account. Relative errors for daily means are about 11%, and decrease to 6% for monthly means.

We have calculated annual records of cloud optical thickness for each of the six locations considered in this study. It shows that both in Greenland and Antarctica, clouds become optically thinner and clear-sky conditions more frequent away from the coast. A smaller precipitable water column at higher altitude and with lower temperatures can explain these findings. Moreover,  $\tau$  increases throughout the summer both in Antarctica and Greenland, which reduces the effect that low ice albedos have on the shortwave radiation balance.

Three applications were presented to demonstrate the versatility of the method. Using  $\tau$  as a selection criterion, it is possible to distinguish between clear and cloudy days, and assess the influence of clouds on, e.g. the radiation budget and snow and ice albedo. Although clouds do attenuate shortwave radiation due to reflection and absorption, the incoming solar radiation at the surface is partly compensated for this loss by multiple reflections between the surface and the cloud base. Averaged over all summer days, multiple reflection enhances  $SW_\downarrow$  by 18% (S5) to 29% (Neumayer) relative to the situation without multiple reflections. Furthermore, we have shown that over snow surfaces, albedo under cloudy sky is always higher than the clear-sky albedo, due to the 'spectral effect' of clouds. Over ice surfaces, this difference ceases, since the visible albedo of ice is so low that the 'spectral effect' that dominates over snow is very weak over ice. As a third application, we detected a statistically significant trend of decreasing  $\tau$  from the 1995–2004 Neumayer data series, consistent with a reported increase in incoming solar radiation. The method is thus suitable to detect long-term trends in the optical properties of clouds over snow and ice.

The use of the methods presented in this paper is not restricted to glaciers and ice sheets. It can be

applied to any snow or ice surface, as long as radiation measurements are reasonably reliable. This opens up possibilities to explore data records from seasonally snow-covered regions in the Arctic. Although not tested in this manuscript, the method could even be applicable to radiation data over any surface. For that, the coefficients derived by Fitzpatrick *et al.* (2004) should be rederived using spectral albedos typical for that surface.

## Acknowledgements

We would like to thank the technical staff of the IMAU for designing, building, and maintaining the AWSs, especially Wim Boot, Henk Snellen, Marcel Portanger, Paul Smeets, and Janneke Ettema. Gert König-Langlo from the Alfred Wegener Institute (AWI) in Bremerhaven, Germany, is kindly thanked for providing and discussing the Neumayer data set. Piet Stammes (KNMI), Wouter Greuell (KNMI) and an anonymous reviewer are kindly thanked for their constructive remarks.

## References

- Allison I, Wendler G, Radok U. 1993. Climatology of the East Antarctic ice sheet (100 E to 140 E) derived from automatic weather stations. *Journal of Geophysical Research* **98**(D5): 8815–8823.
- Ambach W. 1974. The influence of cloudiness on the net radiation balance of a snow surface with high albedo. *Journal of Glaciology* **13**(67): 73–84.
- Ångström A, Tryselius O. 1934. Total radiation from sun and sky at Abisko. (68 21'.2 N, 18 49'.3 E). *Geografiska Annaler* **16**: 53–69.
- Bintanja R, van den Broeke MR. 1996. The influence of clouds on the radiation budget of ice and snow surfaces in Antarctica and Greenland in summer. *International Journal of Climatology* **16**: 1281–1296.
- Box JE, Bromwich DH, Veenhuis BA, Bai L-S, Stroeve JC, Rogers JC, Steffen K, Haran T, Wang S-H. 2006. Greenland ice sheet surface mass balance variability (1988–2004) from calibrated polar MM5 output. *Journal of Climate* **19**: 2783–2800.
- Brock BW, Willis IC, Sharp MJ. 2000. Measurement and parameterization of albedo variations at Haut Glacier d'Arolla, Switzerland. *Journal of Glaciology* **46**(155): 675–688.
- Duchon CE, O'Malley MS. 1999. Estimating cloud type from pyranometer observations. *Journal of Applied Meteorology* **38**: 132–141.
- Dürr B, Philipona R. 2004. Automatic cloud amount detection by surface longwave downward radiations measurements. *Journal of Geophysical Research* **109**: D05201, DOI:10.1029/2004JD004182.
- Dyrgerov M, Meier MF. 2005. *Glaciers and the Changing Earth System: A 2004 Snapshot*, Occasional paper 58, Institute of Arctic and Alpine Research: Boulder; 118 pp.
- Fitzpatrick MF, Brandt RE, Warren SG. 2004. Transmission of solar radiation by clouds over snow and ice surfaces: a parameterization in terms of optical depth, solar zenith angle, and surface albedo. *Journal of Climate* **17**: 266–275.
- Giesen RH, Andreassen LM, van den Broeke MR, Oerlemans J. 2009. Comparison of the meteorology and surface energy balance at Storöen and Midtdalsbreen, two glaciers in southern Norway. *The Cryosphere* **3**: 57–74.
- Greuell W, Knap WH, Smeets CJPP. 1997. Elevational changes in meteorological variables along a midlatitude glacier during summer. *Journal of Geophysical Research* **102**(D22): 25941–25954.
- Greuell W, Oerlemans J. 2004. Narrowband-to-broadband albedo conversion for glacier ice and snow: equations based on modeling and ranges of validity of the equations. *Remote Sensing of Environment* **89**: 95–105.
- Griggs JA, Bamber JL. 2008. Assessment of cloud cover characteristics in satellite datasets and reanalysis products for Greenland. *Journal of Climate* **21**: 1837–1849.
- Hoch SW. 2005. Radiative flux divergence in the surface boundary layer. A study based on observations at Summit, Greenland, Ph.D. thesis, Swiss Federal Institute of Technology, Zürich.

- Jonsell U, Hock R, Holmgren B. 2003. Spatial and temporal variations in albedo on Storglaciären, Sweden. *Journal of Glaciology* **49**(164): 59–68.
- Knap WH, Reijmer CH, Oerlemans J. 1999. Narrowband to broadband conversion of Landsat-TM glacier albedos. *International Journal of Remote Sensing* **20**(10): 2091–2110.
- Konzelmann T, van de Wal RSW, Greuell W, Bintanja R, Henneken EAC, Abe-Ouchi A. 1994. Parameterization of global and longwave incoming radiation for the Greenland Ice Sheet. *Global and Planetary Change* **9**: 143–164.
- Kuipers Munneke P, Reijmer CH, van den Broeke MR, Stammes P, König-Langlo G, Knap WH. 2008. Analysis of clear-sky Antarctic snow albedo using observations and radiative transfer modeling. *Journal of Geophysical Research* **113**: D17118, DOI:10.1029/2007JD009653.
- Liljequist GH. 1956. Energy exchange of an Antarctic snow field: Short-wave radiation (Maudheim 71° 03' S, 10° 56' W) *Norwegian-British-Swedish Antarctic Expedition, 1949-52, Scientific Results*, vol. 2, part 1A, Norsk Polarinstitut: Oslo.
- Long CN, Ackerman TP. 2000. Identification of clear skies from broadband pyranometer measurements and calculation of downwelling shortwave cloud effects. *Journal of Geophysical Research* **105**(D12): 15609–15626.
- Maresh A, Walden VP, Warren SG. 2001. Ground-based infrared remote sensing of cloud properties over the Antarctic plateau. Part II: cloud optical depths and particle sizes. *Journal of Applied Meteorology* **40**: 1279–1294.
- Marty C, Philipona R. 2000. The clear-sky index to separate clear-sky from cloudy-sky situations in climate research. *Geophysical Research Letters* **27**(17): 2649–2652.
- Meyers TP, Dale RF. 1983. Predicting daily insolation with hourly cloud height and coverage. *Journal of Climate and Applied Meteorology* **22**: 537–545.
- Michel D, Philipona R, Ruckstuhl C, Vogt R, Vuillemier L. 2008. Performance and uncertainty of CNR1 net radiometers during a one-year field comparison. *Journal of Atmospheric and Oceanic Technology* **25**: 442–451.
- Ohmura A, Dutton EG, Forgan B, Fröhlich C, Gilgen H, Hegner H, Heimo A, König-Langlo G, McArthur B, Müller G, Philipona R, Pinker R, Whitlock CH, Dehne K, Wild M. 1998. Baseline Surface Radiation Network (BSRN/WCRP): new precision radiometry for climate research. *Bulletin of the American Meteorological Society* **79**(10): 2115–2136.
- Ricchiazzi P, Gautier C, Lubin D. 1995. Cloud scattering optical depth and local surface albedo in the Antarctic: simultaneous retrieval using ground-based radiometry. *Journal of Geophysical Research* **100**(D10): 21091–21104.
- Rignot E, Bamber JL, van den Broeke MR, Davis C, Li Y, van de Berg WJ, van Meijgaard E. 2008. Recent Antarctic ice mass loss from radar interferometry and regional climate modelling. *Nature Geoscience* **1**: 106–110.
- Schneider SH, Dickinson RE. 1976. Parameterization of fractional cloud amounts in climatic models: the importance of modeling multiple reflections. *Journal of Applied Meteorology* **15**: 1050–1056.
- Shepherd A, Wingham D. 2007. Recent sea-level contributions of the Antarctic and Greenland ice sheets. *Science* **315**: 1529–1532.
- Shine KP. 1984. Parameterisation of the shortwave flux over high albedo surfaces as a function of cloud thickness and surface albedo. *Quarterly Journal of the Royal Meteorological Society* **110**: 747–764.
- Stearns CR, Wendler G. 1988. Research results from Antarctic automatic weather stations. *Reviews of Geophysics* **26**(1): 45–61.
- Stephens GL. 1984. The parameterization of radiation for numerical weather prediction and climate models. *Monthly Weather Review* **112**: 826–867.
- Town MS, Walden VP, Warren SG. 2007. Cloud cover over the South Pole from visual observations, satellite retrievals, and surface-based infrared radiation measurements. *Journal of Climate* **20**: 544–559.
- Van den Broeke MR, Reijmer CH, van de Wal RSW. 2004a. Surface radiation balance in Antarctica as measured with automatic weather stations. *Journal of Geophysical Research: Series D* **109**: D09103, DOI:10.1029/2003JD004394.
- Van den Broeke MR, van As D, Reijmer CH, van de Wal RSW. 2004b. Assessing and improving the quality of unattended radiation observations in Antarctica. *Journal of Atmospheric and Oceanic Technology* **21**: 1417–1431.
- Van den Broeke MR, Bamber J, Ettema J, Rignot E, Schrama E, van de Berg WJ, van Meijgaard E, Velicogna I, Wouters B. 2009. Partitioning recent Greenland mass loss. *Science* **326**: 984–986.
- Van den Broeke MR, Smeets CJPP, Ettema J, Kuipers Munneke P. 2008. Surface radiation balance in the ablation zone of the West Greenland ice sheet. *Journal of Geophysical Research: Series D* **113**: D13105, DOI:10.1029/2007JD009283.
- Wild M, Gilgen H, Roesch A, Ohmura A, Long CN, Dutton EG, Forgan B, Kallis A, Russak V, Tsvetkov A. 2005. From dimming to brightening: decadal changes in solar radiation at Earth's surface. *Science* **308**: 847–850.
- Wiscombe WJ, Warren SG. 1980. A model for the spectral albedo of snow. I: pure snow. *Journal of the Atmospheric Sciences* **37**: 2712–2733.
- Zeng Q, Cao M, Feng X, Liang F, Chen X, Sheng W. 1984. A study of spectral reflection characteristics for snow, ice and water in the north of China. In *Hydrological Applications of Remote Sensing and Remote Data Transmission*, vol. 145, Goodison BE (ed). IAHS: Wallingford, UK; 451–462.